lubricants

MDPI

Article

Effect of Structural Flexibility of Wheelset/Track on Rail Wear

Bingguang Wen [1], Gongquan Tao [1], Xuguang Wen [2], Shenghua Wang [3,4] and Zefeng Wen [1,*]

1 State Key Laboratory of Traction Power, Southwest Jiaotong University, Chengdu 610031, China
2 Guangxi China-ASEAN (Association of Southeast Asian Nations) International Joint Key Laboratory of Integrated Transportation, Nanning University, Nanning 541699, China
3 School of Mechanical Engineering, Southwest Jiaotong University, Chengdu 610031, China
4 Shanghai Shentong Metro Group Co., Ltd., Shanghai 201103, China
* Correspondence: zfwen@swjtu.edu.cn

Abstract: To investigate the influence of the structural deformation of the wheelset and track on rail wear in the longitudinal and lateral directions, a rail wear prediction model is established that can calculate the three-dimensional distribution of rail wear. The difference between the multi-rigid-body dynamic model and the rigid-flexible coupled dynamic model, which considers the structural flexibility of the wheelset and track, is compared in terms of the three-dimensional distribution of rail wear. The results show that the three-dimensional distributions of rail wear predicted by the two models are relatively similar. There is no obvious difference in the wear band, and the rail wear in the longitudinal direction is almost identical. The cross sections of the worn rail shapes determined by the two models are essentially the same, with a maximum difference of 3.6% in the average value of the wear areas of all cross sections. The track irregularity is the main reason for the uneven distribution of rail wear in the longitudinal direction. The position where the rail wear is more pronounced hardly varies with the evolution of the rail wear. It is recommended to use a multi-rigid-body dynamic model for the prediction of rail wear, which allows both calculation accuracy and efficiency.

Keywords: wheelset; track; structural flexibility; rail wear prediction; three-dimensional wear distribution

check for updates

Citation: Wen, B.; Tao, G.; Wen, X.; Wang, S.; Wen, Z. Effect of Structural Flexibility of Wheelset/Track on Rail Wear. *Lubricants* **2023**, *11*, 231. https://doi.org/10.3390/lubricants11050231

Received: 8 April 2023
Revised: 11 May 2023
Accepted: 18 May 2023
Published: 21 May 2023

1. Introduction

The wheel–rail pair is a critical element in the railway system, and its rolling contact behavior plays a key role in determining the quality of train operation, ensuring operational safety, and controlling transportation costs [1]. However, this contact behavior inevitably leads to wear problems. In recent years, wheel–rail wear problems have become more serious due to the increase in train speed and axle load. For example, rail side wear on small radius curves can reduce rail life to less than three years [2], while wheel flange wear can cause reprofiling intervals to drop from 200,000 to 30,000 km [3]. Such wear problems can eventually lead to increased operating and maintenance costs. Numerical simulations can be used to quickly and effectively to predict the evolution of wheel–rail wear and support the development of more economical and reasonable maintenance schedules [4].

Simulation methods for wheel–rail wear can be divided into two categories: data-driven [5,6] and model-based [7–16] approaches. Although the data-driven approach has higher accuracy and faster computation speed, it requires a large amount of historical data and is often applicable only to specific operational scenarios [17]. Most research on wheel–rail wear prediction currently uses the model-based approach. This paper focuses on the model-based approach based on multibody simulation (MBS), which provides easy access to wheel–rail contact parameters under different operating conditions. The MBS-based approach for numerical prediction of wheel–rail wear consists of four tasks: vehicle dynamic model, wheel–rail local contact model, wear model, and profile updating and smoothing strategy. The MBS-based wheel–rail wear prediction method is currently considered a mature and reliable approach. Extensive validations have been performed and simulation results have been shown to be consistent with measured wear results [2,12–16]. In addition, this method has been widely used in areas such as wheel–rail profile optimization [18–20] and wheel–rail life prediction [2,21].

The dynamic model is an important submodel for predicting wheel–rail wear. In numerical studies of wheel–rail wear, several researchers have used multi-rigid-body dynamic models to improve computational efficiency [10–17]. These models treat the vehicle and track structures as rigid bodies and neglect their elastic deformation. However, the wheel–rail contact is not completely rigid and exhibits some degree of elastic deformation. Previous studies have shown that the deformation of the wheel and rail cannot be ignored. In addition, the flexibility of the wheelset and track structures can significantly affect the wheel–rail contact behavior, including the wheel–rail contact position and creep [22,23]. These parameters are the key input variables for the wheel–rail wear prediction models and significantly affect the prediction results. With the rapid development of computer technology, dynamic simulation can now consider the deformation of flexible bodies. Therefore, researchers are increasingly recognizing the influence of wheelset–track flexibility on wear prediction. Aceituno et al. [24] used the finite element method with floating reference frame to design a flexible rail. Their study showed that the rigid and flexible rail models produced similar results when no track irregularities were present. However, when track irregularities were considered, differences appeared between the two models, and the degree of rail flexibility was found to affect the wear prediction results. Tao et al. [25] investigated the influence of track structure flexibility on wheel wear prediction and found that there was no significant difference in the range of wheel wear between the rigid and flexible track models, but the maximum depth of wheel wear was greater for the rigid track model than for the flexible model. Shi et al. [26] established a wear prediction model based on a vehicle–track coupled dynamic model, considering the track flexibility, and investigated the effect of railpad stiffness on wheel wear prediction. They found that the wheel–rail contact position became more concentrated with increasing stiffness, while the wheel wear decreased with decreasing stiffness. Guo et al. [27] compared flexible and rigid wheelsets in terms of wheel wear prediction and found that both models produced almost identical shapes of wear distribution. However, the flexible wheelset caused higher wheel wear than the rigid wheelset. Refs. [24–27] focused on the influence of wheelset–track flexibility on the lateral wear distribution at the wheel–rail interface. It is noteworthy that the rail experiences both lateral and longitudinal wear, such as the occurrence of rail corrugation, which is a common form of longitudinal wear that can significantly affect railway performance and safety. Refs. [28,29] investigated the influence of wheelset flexibility on the prediction of rail corrugation. However, these studies focused only on the periodic wear distribution of wear depth at a specific lateral position on the rail cross section and did not address the three-dimensional wear distribution of the rail in the longitudinal and lateral directions.

The presence of track irregularities affects the distribution of rail lateral wear, leading to visible variations in different longitudinal positions. As a result, rail wear exhibits specific three-dimensional distribution characteristics in the longitudinal and lateral directions. Previous studies have investigated the influence of wheelset–track structure flexibility on the prediction of rail lateral wear or rail corrugation. However, the specific influence of wheelset and track structure deformation on the three-dimensional distribution of rail wear remains unclear. To solve this problem, this paper presents a rail wear prediction model to calculate the three-dimensional distribution of rail wear in the longitudinal and lateral directions. By combining SIMPACK with ANSYS software, a rigid-flexible coupled dynamic model is developed that takes into account the flexibility of the wheelset and track structures. To investigate the effect of wheel and track flexibility on rail wear prediction, the rigid-flexible coupled dynamic model is compared with a multi-rigid-body dynamic model in terms of model complexity, calculation results, and computational efficiency.

2. Rail Wear Prediction Model

2.1. Three-Dimensional Rail Wear Prediction Process

The rail wear prediction model is a complex mathematical tool that includes a vehicle dynamic model, a wheel–rail local contact model, a wear model, and a profile updating and smoothing strategy. Figure 1 shows the process of predicting the three-dimensional rail wear distribution. The rail wear prediction process is outlined as follows:

(1) The vehicle dynamic model is established using the dynamics software SIMPACK. The track parameters and profiles of wheel and rail are set for dynamic simulation. The wheel–rail contact parameters, such as the lateral position of the rail contact point y_r, the normal force N, the longitudinal creepage ξ_x, the lateral creepage ξ_y, and the spin creepage ξ_ψ, are obtained from output results and used for post-processing.

(2) The contact parameters are used as inputs to the local contact model. The Hertzian theory is used to solve the normal contact to obtain the semi-axes in the rolling direction (a) and lateral direction (b), and the contact pressure distribution. The FASTSIM algorithm [30] is used to obtain the local tangential stress and creep distributions.

(3) The results obtained in the previous step are incorporated into the wear model that uses the $T\gamma/A$-wear rate function based on the rail material U75V [31] to estimate the wear distribution at the contact patch. The wear distributions at different cross sections are determined considering the lateral position y_r of the rail contact points on the different cross sections and the sampling strategy.

(4) The rail wear distribution generated in this iteration is smoothed using the moving average smoothing method. The wear distributions are scaled up for all cross sections according to the predefined updating strategy. In this step, the rail profiles at different longitudinal positions in the normal direction are removed based on the smoothed rail wear distribution. Then, the rail profile obtained after the removal of wear is smoothed using the cubic spline interpolation smoothing method.

(5) The rail profile after wear removal is imported into the vehicle dynamic model for the next iterative calculation. This process is repeated until the simulation requirements are met.

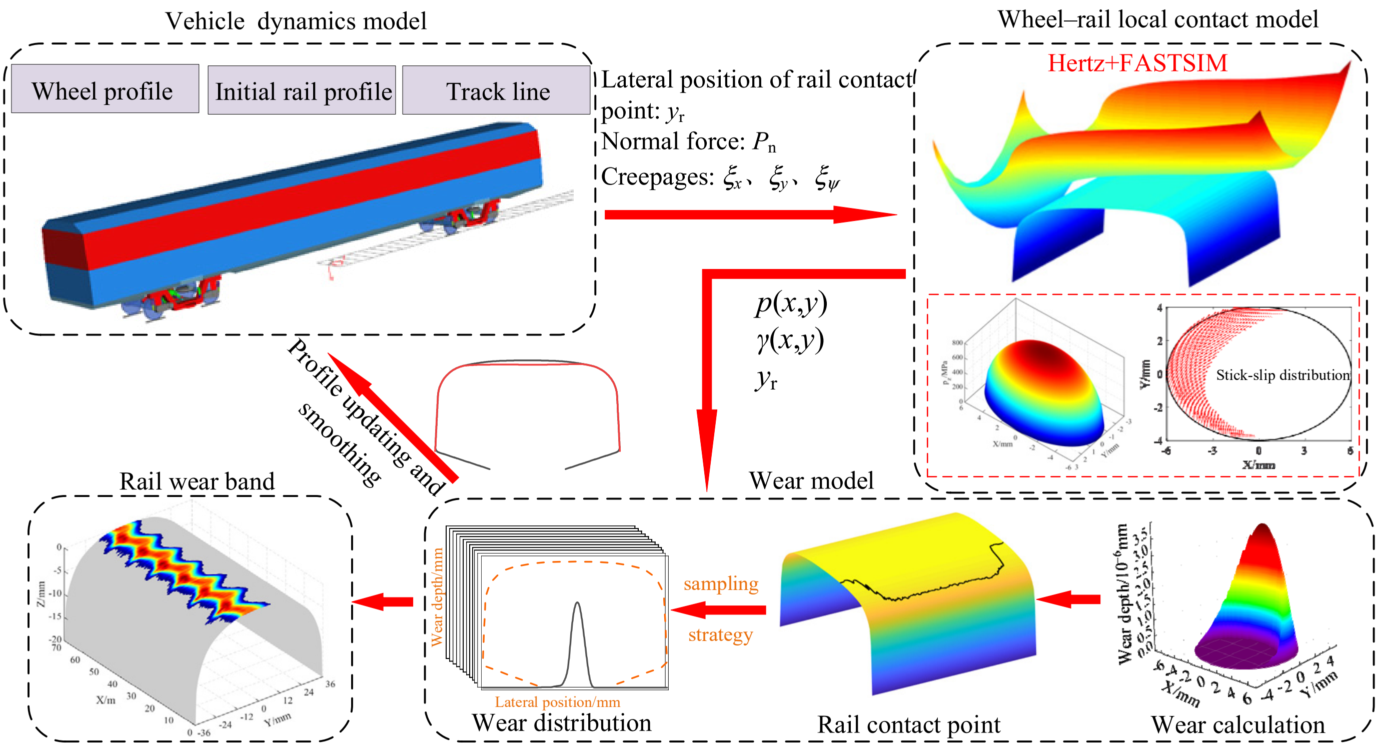

Figure 1. Three-dimensional rail wear prediction process.

The whole process of rail wear prediction in this study is performed automatically using SIMPACK and MATLAB. In addition, some assumptions are made, including:

(1) The evolution of wheel wear is not considered.
(2) The plastic deformation and work hardening during rail wear are not considered.
(3) The influence of vehicle traction and braking on rail wear is ignored.

2.2. Multi-Rigid-Body Dynamic Model

Based on the multibody dynamics software SIMPACK, a multi-rigid-body dynamic model of a trailer vehicle of a type-A metro train is established, which consists of a car body, two bogie frames, four wheelsets, and eight axle boxes. The axle box is modeled with node-type degrees of freedom (DoFs), while the rest of the rigid body structures are modeled with 6 DoFs. Therefore, the multi-rigid-body dynamic model contains a total of 50 DoFs. Some model parameters are listed in Table 1. The vehicle model is shown in Figure 2. The primary suspension system adopts the rotary axle box positioning mode, where a steel spring and vertical damper are used to connect the wheelset and bogie frame. The secondary suspension system comprises two air springs, two traction rods, two vertical dampers, a lateral damper, an antiroll bar, and a lateral bump stop that connects the bogie frame to the car body. Various suspension elements are simplified to equivalent force elements. The nonlinear characteristic of the lateral stop force is also considered. The multi-rigid-body dynamic model is validated using measured wheel–rail contact forces and derailment coefficients [14].

Table 1. Parameters of dynamic model.

Parameter	Value	Units
Car body mass (AW0/AW3)	25,640/50,650	kg
Bogie mass	2800	kg
Wheelset mass	1140	kg
Primary spring longitudinal stiffness	1.4	MN/m
Primary spring lateral stiffness	6.5	MN/m
Primary spring vertical stiffness	1.1	MN/m
Primary vertical damper stiffness	6.4	MN/m
Air spring longitudinal stiffness	0.12	MN/m
Air spring lateral stiffness	0.12	MN/m
Secondary vertical damper stiffness	8	MN/m
Traction rod longitudinal stiffness	13.6	MN/m
Anti-roll bar roll angle stiffness	1.5	MNm/rad
Wheelbase	2.5	m
Wheel rolling-circle diameter	0.84	m

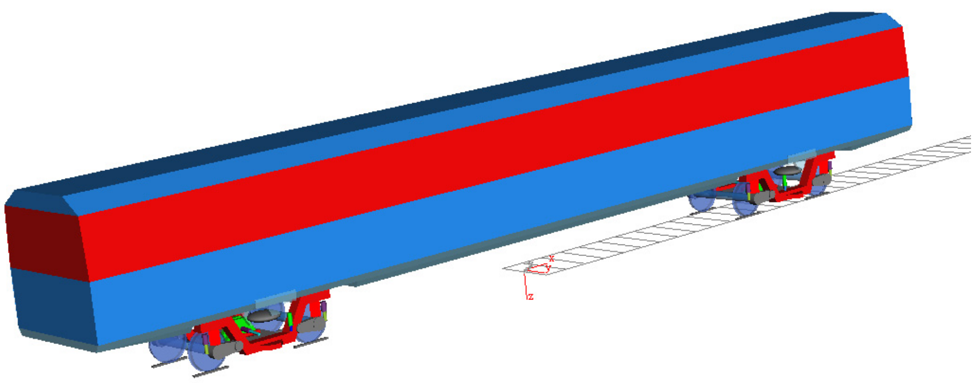

Figure 2. Multi-rigid-body dynamic model.

2.3. Wheel–Rail Local Contact Model

Previous studies have shown that using the Hertzian theory to predict wheel–rail wear remains a compromise [10]. In this work, the Hertzian theory is used to solve the normal problem, and the tangential stress and creep distributions on the contact patch are solved using the FASTSIM algorithm [30]. The implementation process of the FASTSIM algorithm is described below. First, the contact patch is discretized into many grids, as shown in Figure 3, with equidistant strips n_y and n_x along the y-axis and x-axis, respectively. Δx denotes the unit length in the longitudinal direction. The tangential stress is set to zero at the leading edge of the contact patch and is iteratively calculated by the difference from the leading edge to the trailing edge of the contact patch. The recursive expression is as follows:

$$\begin{cases} p_x(x-\Delta x, y_i) = p_x(x, y_i) - \Delta p_x \\ p_y(x-\Delta x, y_i) = p_y(x, y_i) - \Delta p_y \end{cases} \tag{1}$$

where Δp_x and Δp_y are the longitudinal and lateral tangential stress increments, respectively, of the adjacent element nodes. The tangential stress at node ($x - \Delta x$, y_i) is expressed as follows:

$$p_t(x-\Delta x, y_i) = \sqrt{[p_x(x-\Delta x, y_i)]^2 + [p_y(x-\Delta x, y_i)]^2} \tag{2}$$

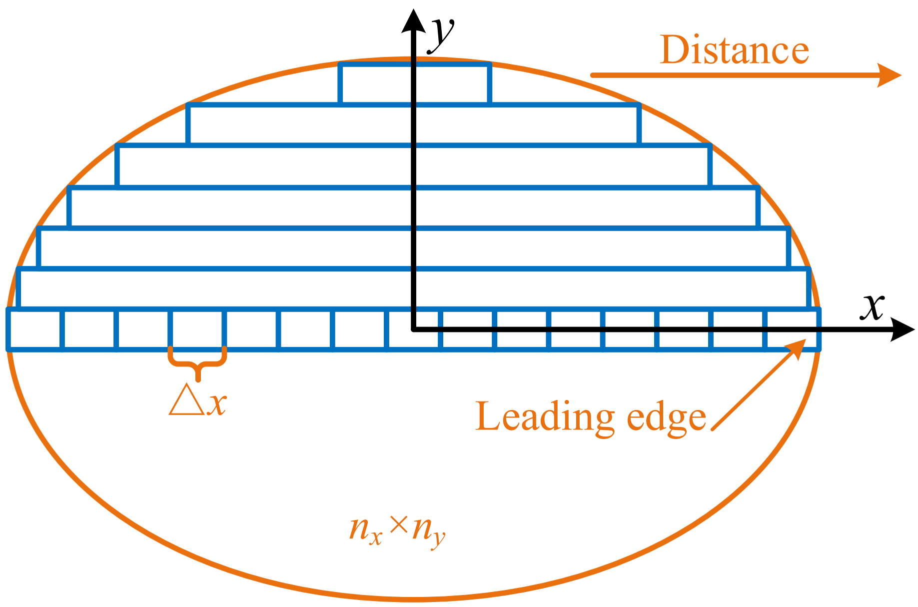

Figure 3. Mesh of contact patch.

Based on Coulomb's law, the judgment condition for the stick or slip condition is as follows:

$$p_t(x-\Delta x, y_i) \le \mu p_3(x-\Delta x, y_i) \tag{3}$$

where μ is the coefficient of friction; $p_3(x - \Delta x, y_i)$ is the contact pressure at the node ($x - \Delta x$, y_i). The FASTSIM algorithm deviates from the Hertzian theory by using a parabolic distribution of the normal contact pressure instead of an ellipsoidal distribution. The calculation expression for the parabolic distribution is presented as follows:

$$p_3(x, y) = \frac{2N}{\pi ab}\left[1 - \left(\frac{x}{a}\right)^2 - \left(\frac{y}{b}\right)^2\right] \tag{4}$$

If the tangential stress component of a node satisfies the condition given in Formula (3), the node is within the stick area. If, on the other hand, this condition is not satisfied, the node is in the slip area. For nodes located in the slip area, the tangential stress components are expressed using the following equation:

$$\begin{cases} p_{xs}(x-\Delta x, y_i) = [p_x(x, y_i) - \Delta p_x]\frac{\mu p_3(x-\Delta x, y_i)}{p_t(x-\Delta x, y_i)} \\ p_{ys}(x-\Delta x, y_i) = [p_y(x, y_i) - \Delta p_y]\frac{\mu p_3(x-\Delta x, y_i)}{p_t(x-\Delta x, y_i)} \end{cases} \tag{5}$$

If the node is in the stick area, its creep is zero. If it is in the slip condition, according to Ref. [32] and considering the effect of elastic deformation on creep, the local creep $\omega_{x,y}$ can be expressed as follows:

$$\begin{cases} \omega_x = \frac{L_x}{\Delta x}[p_{xs}(x-\Delta x, y_i) - p_x(x-\Delta x, y_i)] \\ \omega_y = \frac{L_y}{\Delta x}[p_{ys}(x-\Delta x, y_i) - p_y(x-\Delta x, y_i)] \end{cases} \tag{6}$$

where L_x and L_y are the tangential flexibility parameters in the longitudinal and lateral directions, respectively.

2.4. Wear Model

Grade U75V rail is commonly used in the Chinese metro network. Therefore, the $T\gamma/A$ wear rate function proposed in Ref. [31] for the U75V rail material is used to estimate the rail wear in this study. The $T\gamma/A$ wear rate function of the U75V rail material is based on the twin-disc wear test of the CL60 wheel material and U75V rail material and refers to the form of the widely used USFD wear model [33–35]. The wear map is divided into three regions based on the wear index: mild wear zone (K_1), severe wear zone (K_2), and catastrophic wear zone (K_3), as shown in Figure 4. It is noteworthy that the wear rate shows a linear relationship with $T\gamma/A$ in all three regions, with the largest slope in the catastrophic wear zone. The expressions of the $T\gamma/A$ wear rate function in the three regions are given below [31]:

$$K_w = \begin{cases} 0.3 + 2.59I_w & I_w < 14 \\ 0.16I_w + 34.02 & 14 \le I_w < 66 \\ 10.86I_w - 672.18 & I_w \ge 66 \end{cases} \tag{7}$$

where K_w (units: $\mu g/(m \cdot mm^2)$) represents the mass of material removed for a unit distance travelled on the unit area of the contact patch. Meanwhile, I_w (units: N/mm^2) represents the friction work of the elements in the contact patch, which can be calculated based on the wear index as follows:

$$I_w(x, y) = p(x, y) \cdot \gamma(x, y) \tag{8}$$

where $p(x, y)$ and $\gamma(x, y)$ represent the tangential stress and creep in each element (x, y) of the contact patch, respectively.

In this study, the contact patch is discretized in 40×40 grids. The tangential stresses and creep of the cells within the contact patch are calculated using the FASTSIM algorithm. After determining the wear rate K_w by Equation (7), the wear depth of each element within the contact patch can be determined by the following equation:

$$\delta(x, y) = \frac{K_w}{\rho}\Delta x \tag{9}$$

where ρ (units: kg/m^3) represents the density of the rail material.

After calculating the wear depth for each cell, the wear depth at the lateral position y in the contact patch is accumulated longitudinally to determine the transverse wear distribution on the contact patch:

$$\delta(y) = \int_{-a(y)}^{+a(y)} \delta(x, y)\mathrm{d}x \tag{10}$$

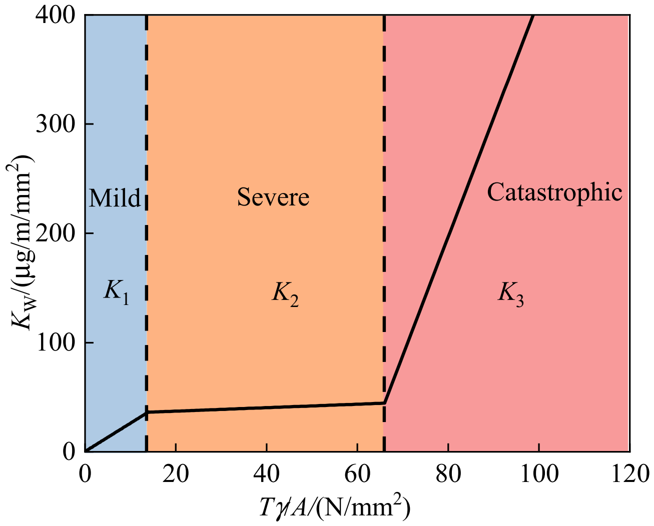

Figure 4. $T\gamma/A$ wear rate curve.

2.5. Sampling and Updating Strategy

In this study, a sampling strategy is used to calculate the three-dimensional distribution of rail wear, as shown in Figure 5. Since wear is gradual due to the plastic flow of materials, there are negligible differences in the wheel–rail force and wear distribution for closely spaced sections [36]. To improve simulation efficiency, the wear calculations are performed on sections spaced at fixed intervals. The distribution of wear calculation sections is shown in blue in Figure 5. The spacing between adjacent wear cross sections, denoted as d_c, is set to 0.25 m, following Refs. [36,37]. In addition, the distance between dynamic sampling points, d_m, is set to 25 mm, which means that the dynamic parameters are extracted every 25 mm to calculate the wear. One sampling is performed to calculate the rail wear caused by a single passage of the wheel. In SIMPACK, the rail profile for adjacent sections of the wear calculation is determined by interpolation. Assuming that the length of the wear calculation area is l, the number of wear calculation sections is expressed as follows:

$$N_c = l/d_c + 1 \tag{11}$$

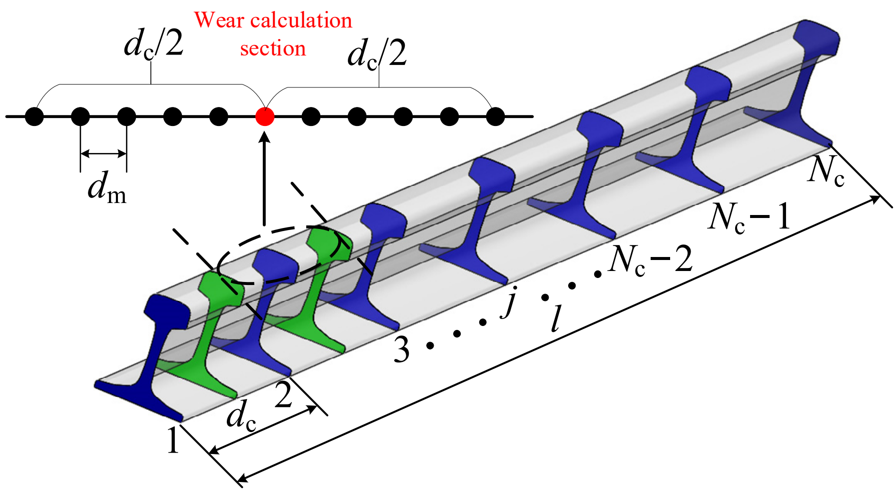

Figure 5. Sampling strategy.

To ensure a smoother calculation of wear, the average wear distribution within each sampling area is considered for each section of the wear calculation. The procedure can be outlined as follows: The sampling area of each wear calculation section covers a distance of

$d_c/2$ before and after it (for the first wear calculation section, the sampling area covers only a distance of $d_c/2$ after it, while for the last section, the sampling area covers only a distance of $d_c/2$ before it). The wear distribution for each wear calculation section is obtained by averaging the rail wear at all dynamic sampling points in its sampling area. The calculation of the wear superposition for each wear calculation section is shown as follows:

$$\begin{cases} \delta^p_{j,\mathrm{L}}(y) = \frac{1}{N_\mathrm{m}} \sum\limits_{i=1}^{N_\mathrm{m}} \sum\limits_{k=1}^{4} \delta^p_{ijk,\mathrm{L}}(y) \\ \delta^p_{j,\mathrm{R}}(y) = \frac{1}{N_\mathrm{m}} \sum\limits_{i=1}^{N_\mathrm{m}} \sum\limits_{k=1}^{4} \delta^p_{ijk,\mathrm{R}}(y) \end{cases} \tag{12}$$

where $\delta^p_{j,\mathrm{L}}(y)$ and $\delta^p_{j,\mathrm{R}}(y)$ represent the left and right rail wear, respectively, caused by one pass of a vehicle through the j-th wear calculation section during the p-th iteration. $\delta^p_{ijk,\mathrm{L}}(y)$ and $\delta^p_{ijk,\mathrm{R}}(y)$ represent the rail wear at the i-th sampling point of the j-th wear calculation section generated by the left and right wheels, respectively, of the k-th wheelset of the vehicle during the p-th iteration. N_m denotes the number of dynamic sampling points within the wear calculation section. In particular, it is equal to $d_c/d_m + 1$, except for the first and last wear calculation sections, where the expression is $d_c/(2d_m) + 1$. i represents the i-th sampling point, $i = 1 - N_\mathrm{m}$. j represents the j-th wear calculation section, $j = 1 - N_c$. k represents the k-th wheelset of the vehicle, k = 1–4.

During actual operation, the wheels of the passing train continuously wear the rail, resulting in real-time changes of the rail profile. However, updating the rail profile in real-time numerical simulations can be challenging. Therefore, it is necessary to develop a suitable updating strategy to amplify the rail wear caused by one passing vehicle through Equation (12). In predicting the rail wear, the profile updating strategy is usually based on the maximum wear depth or the number of wheel passes (vehicle passes). To provide an intuitive comparison between the rigid-flexible and rigid models in predicting rail wear, an updating strategy of 10,000 wheel passes (or 2500 vehicle passes) was used in this study. At each iteration, the left (or right) rail wear of each wear calculation section was first calculated using Equation (12). Then, the calculated wear was amplified based on the updating strategy of 2500 vehicle passes. The resulting increase in rail wear for the j-th wear calculation section in the p-th iteration can be expressed as follows:

$$\overline{\delta}^p_{j,\mathrm{L}}(y) = 2500 \times \delta^p_{j,\mathrm{L}}(y);\ \overline{\delta}^p_{j,\mathrm{R}}(y) = 2500 \times \delta^p_{j,\mathrm{R}}(y) \tag{13}$$

Finally, using the rail profile obtained from the previous iteration, the wear in the normal direction is removed for all rail profiles at different longitudinal positions based on the wear distribution of their respective cross sections after updating.

3. Flexibility of Wheelset and Track Structure

3.1. Flexibility of Wheelset

ANSYS is used to build a finite element model of a wheelset for a type-A metro vehicle. The wheelset is meshed with Solid185 elements with a Young's modulus of 206 GPa, Poisson's ratio of 0.28, and density of 7790 kg/m^3. To simplify the integral calculation, the DoFs of the wheelset model must be reduced. Typically, this requires performing a substructure analysis of the wheelset using ANSYS and applying the Guyan reduction method [38] to derive the reduction matrix solution of the wheelset. In this study, 235 master nodes were selected for substructure analysis, as shown in Figure 6. Among them, 160 master nodes were assigned for nominal rolling circle sections and spokes of the wheel on both sides. A total of 13 axle sections with 2 primary force positions were included, with 5 master nodes selected for each axle section and 10 master nodes selected for each wheel hub on both sides. All master nodes had 6 DoFs.

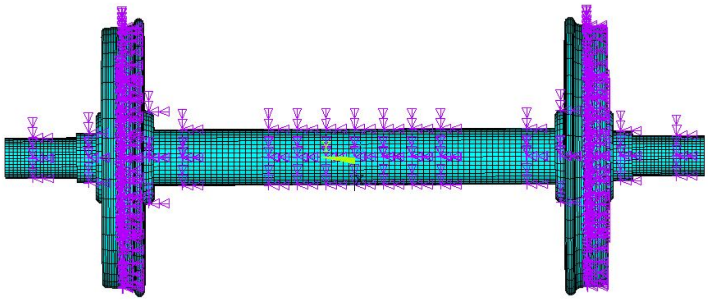

Figure 6. Wheelset master nodes.

To ensure the accuracy of the wheelset substructure model after reduction, the Block Lanczos method in ANSYS was used to extract the first six vibration modes of the wheelset model in the free state. The difference between the mode calculation results of the finite element model of the wheelset and the substructure model was compared, and the relative error is shown in Table 2. From Table 2, it can be seen that in the first six orders of the wheelset modes, the difference between the calculation results of the original wheelset modes and the substructure analysis modes is negligible, with a maximum difference of only 0.41%. This indicates that the wheelset substructure model established in this work is accurate. The flexible body file (.fbi) of the wheelset was generated using the FEMBS interface of SIMPACK. During simulation, the first five modes were selected with an appropriate cutoff frequency of 250 Hz.

Table 2. Modal calculation results of wheelset.

Mode Descriptions (Order)	Original Model (Hz)	Substructure (Hz)	Relative Error (%)	Mode Shapes
1st Torsion (1)	88.914	88.93	0.02	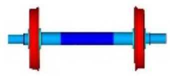
1st Bending (2 and 3)	104.953/104.954	104.993/104.994	0.04/0.04	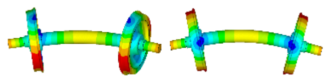
2nd Bending (4 and 5)	201.001/201.003	201.252/201.253	0.12/0.12	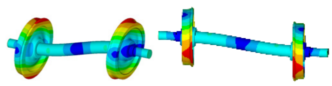
Umbrella deformation (6)	381.06	382.604	0.41	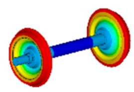

3.2. Flexibility of Track

Finite element models of the rail and slab are developed using the finite element software ANSYS. The rail is modeled as a Timoshenko beam supported by continuous elastic discrete points, with mesh generation performed using the Beam188 element. The slab is simplified into a hexahedral structure with dimensions of 5 m $\times$ 0.3 m in width and height, respectively, and the dimension in the longitudinal direction is determined based on the length of the flexible track to be designed. A Solid185 element is used for mesh partitioning, and 8-node hexahedral solid elements are used for meshing. To improve the computational efficiency, it is also necessary to select the master node for the finite element model of slab and rail to reduce the DoFs of the model. To set the fastener force element constraint in SIMPACK, the master nodes at the fastener connection between the rail and slab are selected every 0.6 m in ANSYS. Similarly, the master nodes at the connection between the bottom surface of the slab and the foundation are selected every 0.6 m to set the slab support force element constraint in SIMPACK. All the master nodes have 6 degrees of freedom. Some parameters of the track structure are listed in Table 3.

Table 3. Parameters of track structure.

Parameters	Value	Unit
Fastener spacing	0.6	m
Slab support spacing	0.6	m
Rail	60	kg/m
Young's modulus of slab	32.5	GPa
Poisson's ratio of slab	0.24	-
Density of slab	2400	kg/m^3
Fastener vertical stiffness	60	MN/m
Fastener vertical damping	60	kN·s/m
Slab support vertical stiffness	170	MN/m
Slab support vertical damping	31	kN·s/m

After the finite element model of the rail and slab is established, the corresponding Flextrack configuration file (.Ftr) needs to be prepared, which mainly contains visual information, fastener stiffness and damping, slab support constraints, and the position information of the master nodes of the left and right rails. Then, the flexible rail model is imported via the Flextrack module of SIMPACK and the wheel–rail contact pair is modified. The flexible body file (.fbi) of the slab is generated using the FEMBS interface of SIMPACK, and then imported. The fastener and slab support force element constraints are defined in SIMPACK. To simulate the interaction between the flexible rail and the flexible slab, an elastic support layer is incorporated and discretized into a set of spring-damping elements to model the fastener force, considering its stiffness and damping in three translational directions. To capture the rolling deformation of the rail and account for its stiffness and damping around the longitudinal rotation, it is modeled with the force element 43 in SIMPACK. Similarly, a series of spring-damping elements are used to connect the flexible slab and the foundation to simulate the slab support, taking into account its stiffness and damping in three translational directions and expressed by force element 5 in SIMPACK. During the simulation, the first 200 Hz mode is intercepted by the flexible slab. Figure 7 shows some mode shapes of the flexible slab.

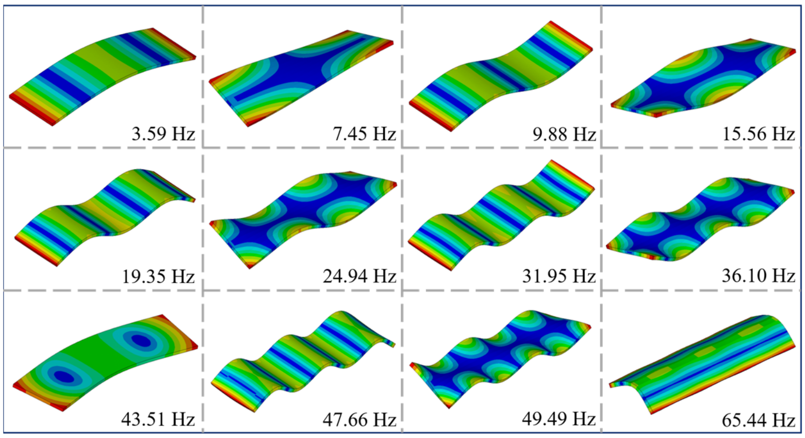

Figure 7. Some mode shapes of the slab.

3.3. Verification of Rigid-Flexible Coupled Dynamic Model

In this work, the multi-rigid-body dynamic model presented in Section 2.2 was extended to include the flexibility of the wheelset and track, forming a rigid-flexible coupled dynamic model, as shown in Figure 8. The model was verified using measured wheel–rail force data on the R1200 curve, with track parameters selected based on the actual track, including a flexible curve track length of 129 m, a circular curve length of 49 m, a transition curve length of 40 m, and a curve superelevation of 50 mm. The vehicle speed was set to 80 km/h, the American level-6 spectrum was used for the track irregularities, and the car body loading was set to AW0 status. The verification results for the vertical and lateral forces are shown in Figure 9, and show good agreement between the simulated and measured forces. Thus, the rigid-flexible coupled dynamic model is considered accurate and reliable.

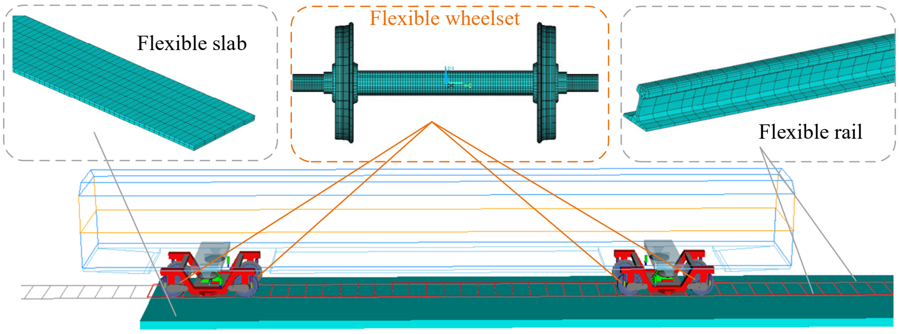

Figure 8. Rigid-flexible coupled dynamic model.

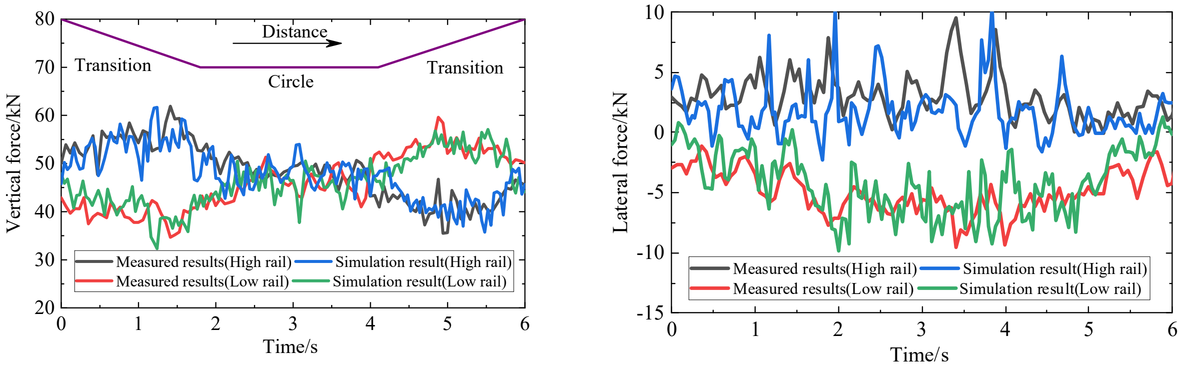

(**a**) Vertical force (**b**) Lateral force

Figure 9. Model validation.

4. Analysis of Simulation Results

In this study, two different operating scenarios were investigated, namely, straight and curved tracks. During the simulation process, the car body loading was set to AW3 status with a running speed of 60 km/h. The American level-6 track irregularity spectrum was used, and the rail cant was set to 1:40. The length of the flexible track was 50 m for the straight track case. For the curved scenario, a left curve was simulated with the left rail serving as the high rail and the right rail serving as the low rail. The total length of the curve was 135 m, with a flexible track length of 45 m for the transition and the circular curve. The curve radius was 600 m with a curve superelevation of 70 mm. The wheel profile used in the simulation corresponded to the standard profile LM, while the standard rail profile CHN60 was used.

4.1. Lateral Position Distribution of Rail Contact Point

The lateral position of the rail contact point is a necessary parameter for determining the cross section wear region when predicting rail wear. In multibody dynamic models, this position is determined by the static contact between the wheel and the rail. However, in the rigid-flexible coupled dynamic model, which takes into account the deformation of both the wheelset and the track, the position necessarily changes compared to the multi-rigid-body dynamic model, which requires an analytical investigation. Figure 10 illustrates the distribution of the position of the rail contact point for two models in the straight and curved cases. For the left rail (high rail), a positive value indicates the lateral position on the gauge side, while a negative value indicates the lateral position on the gauge side for the right rail (low rail). For the straight case, the contact point positions for the left and right rails are mainly concentrated at a distance of about 10 mm from the center of the rail top, and the position may jump to about 20 mm from the center of the rail top for uneven tracks. While the distribution of the rail contact point positions determined by the two models shows little difference, the rigid-flexible coupled dynamic model takes structural deformation into account, resulting in a larger range of variation in contact point position under the influence of track irregularities. For the curved case, both models show similar distribution patterns for the high rail contact point positions, but some discrepancies are observed for the low rail contact point positions, especially in the circular curve. Notably, the rigid-flexible coupled dynamic model, which incorporates the flexibility of both the wheelset and the track, causes the contact point position of the low rail to shift outward compared to the multibody dynamic model. This is due to the fact that the wheel contacts the rail at the gauge side in the small radius curve, and the gauge dynamically expands due to the wheel–rail forces, resulting in a larger lateral displacement of the wheelset and, consequently, a shift in the position of the contact point of the low rail position to the outside of the rail. As shown in Figure 11, the maximum lateral displacement of the wheelset for the rigid-flexible coupled dynamic model under this curved condition without track irregularities is about 8.8 mm, while it is about 7.5 mm for the multibody dynamic model. Figures 10 and 11 show that the rigid-flexible coupled dynamic model, which takes into account the flexibility of the wheelset and the track, exhibits harmonic oscillations in its results, especially under the condition that there are no track irregularities. This can be attributed to the bending deformation of the axle due to the sprung weight, which leads to periodic changes in the wheel tread deviation, with a period of about 0.158 s, which corresponds to the time taken by the wheel to make one revolution.

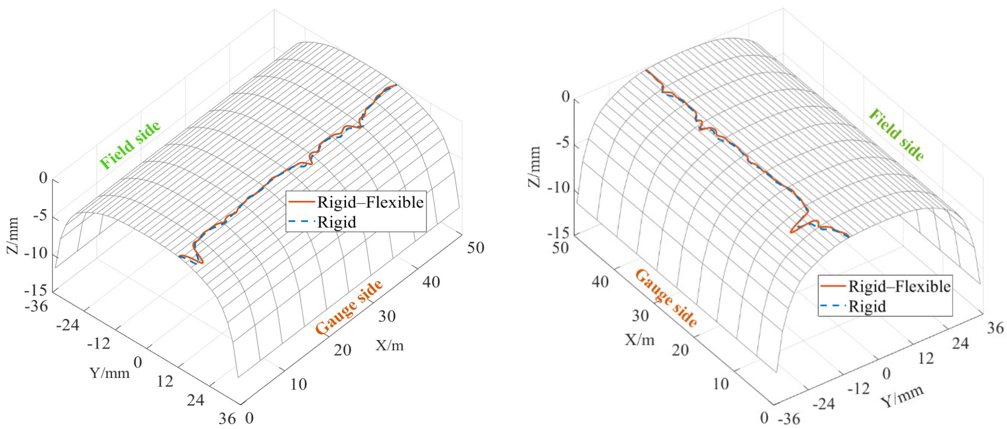

(**a**) Left rail for straight case (**b**) Right rail for straight case

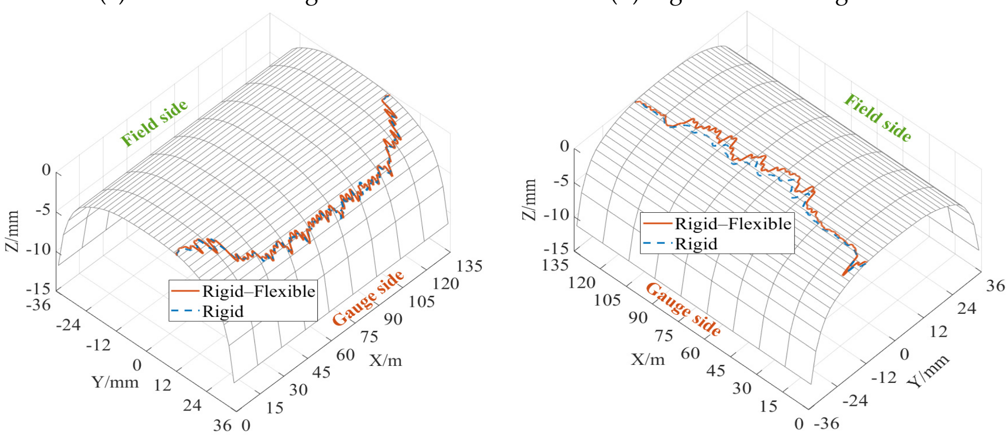

(**c**) Left (high) rail for curved case (**d**) Right (low) rail for curved case

Figure 10. Lateral position distribution of rail contact point.

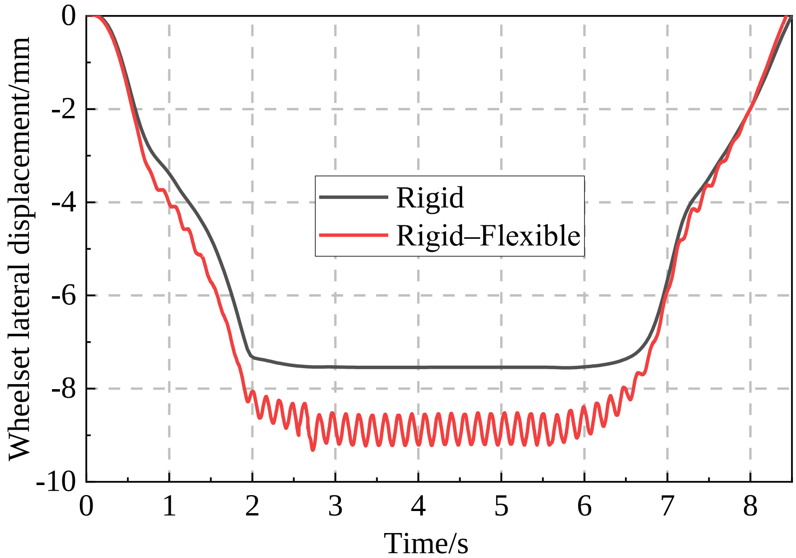

Figure 11. The results of wheelset lateral displacement.

4.2. Three-Dimensional Wear Distribution of Rail

The rail wear caused by continuous train passage is studied through five iterations. Figures 12 and 13 illustrate the differences in the three-dimensional distribution of rail wear between the first and fifth iterations for the straight track case. The gray areas in the figures indicate zero wear. It is worth noting that the two models use the same color bar, and the assumption is made that the wear distribution remains constant between two successive cross sections, thus achieving a continuous simulation representation. The figures show that the track irregularities affect the wear distribution at different longitudinal positions. In particular, the left rail has slightly larger wear depth than the right rail. The wear band on both rails appears relatively straight along the longitudinal position; however, the irregularity increases the wear area on some cross sections. At the first iteration, the width of the wear band is about 8 mm, and the wear is concentrated at a distance of 10–15 mm from the center of the rail top on both rails. At the fifth iteration, the overall wear band resembles that of the first iteration, with the heavily worn areas (indicated in red in the figures) remaining unchanged but increasing slightly in width and amount of wear. Both models exhibit a relatively similar three-dimensional wear distribution, with no significant differences in the variation characteristics of the wear band or the location of the wear peaks. However, the contact point position in the rigid-flexible coupled dynamic model changes abruptly when track irregularities are taken into account, resulting in a slightly wider wear range compared to the multibody dynamic model.

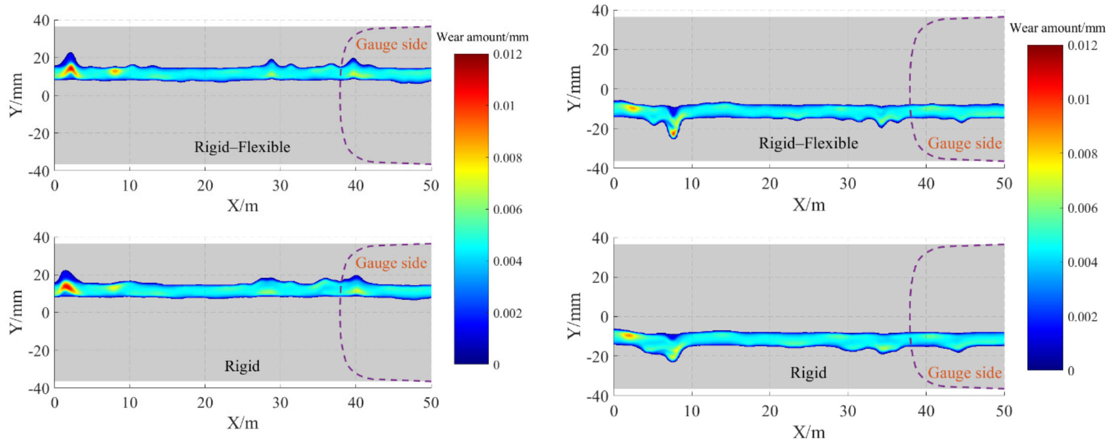

(**a**) Left rail (**b**) Right rail

Figure 12. Rail wear band results after the first iteration (straight case).

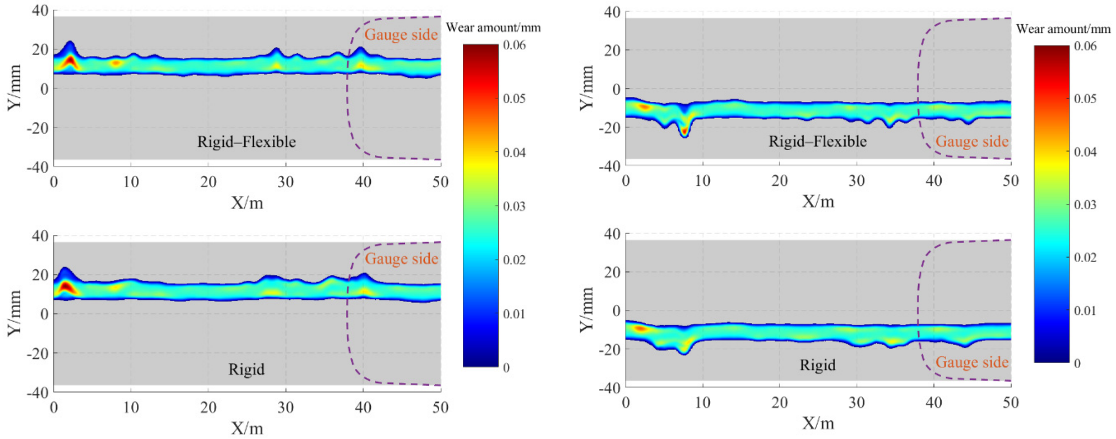

(**a**) Left rail (**b**) Right rail

Figure 13. Rail wear band result after the fifth iteration (straight case).

Figures 14 and 15 show the difference in the three-dimensional wear distribution of the rail between two models for the curved case, corresponding to the first and fifth iterations, respectively. Overall, the wear band characteristics on the whole curve show the phenomenon of increase before decrease, regardless of the high or low rail. The circular curve exhibits the greatest wear. At the transition, differences in radius of curvature and superelevation at different longitudinal positions result in a wear band that exhibits a trumpet-shaped distribution, and the region near the circular curve shows greater wear and a wider wear range. In contrast, the wear bands on the high and low rails of the circular curve are relatively straight and parallel to the longitudinal direction, i.e., the wear distribution characteristics of different cross sections are similar. Initially, two relatively distinct wear bands occur on the high rail in the circular curve, with the lighter band near the gauge corner caused by the leading wheelset contact and the 10−15 mm wide wear band caused by the nonleading wheelset contact. Over time, the area between these bands wears away and becomes a single wear band covering almost the entire inside of the rail. The wear band range of the low rail is mainly in the range of −15–0 mm. Moreover, the fluctuation behavior of the contact point in the rigid-flexible coupled dynamic model leads to a noticeable harmonic fluctuation in the three-dimensional wear distribution of the rail. Comparing the results of the first and fifth iterations, it is clear that the law of wear band evolution for the curved track case is the same as that for the straight track case and is mainly characterized by a widening of the wear band, with the predominant wear region retaining its significance.

Based on the results of the two models, it can be found that there is also no significant difference in the three-dimensional wear distribution of the rail for the case of the curved track. The characteristics of the wear band are also similar, and the longitudinal positions of the areas exhibiting obvious wear are the same for both models. However, compared to the multi-rigid-body dynamic model, the rigid-flexible coupled dynamic model results in a slightly larger total wear depth on the high rail and a slightly smaller depth on the low rail. In addition, the wear area is also larger. This difference can be attributed to the fact that the rigid-flexible coupled dynamic model takes into account the dynamic expansion of the gauge under the small curve radius conditions, which causes the contact point on the high rail to be closer to the gauge corner and experience greater wear. Conversely, the contact point on the low rail shifts outward toward the top center of the rail, resulting in a larger contact area and, thus, a larger wear area.

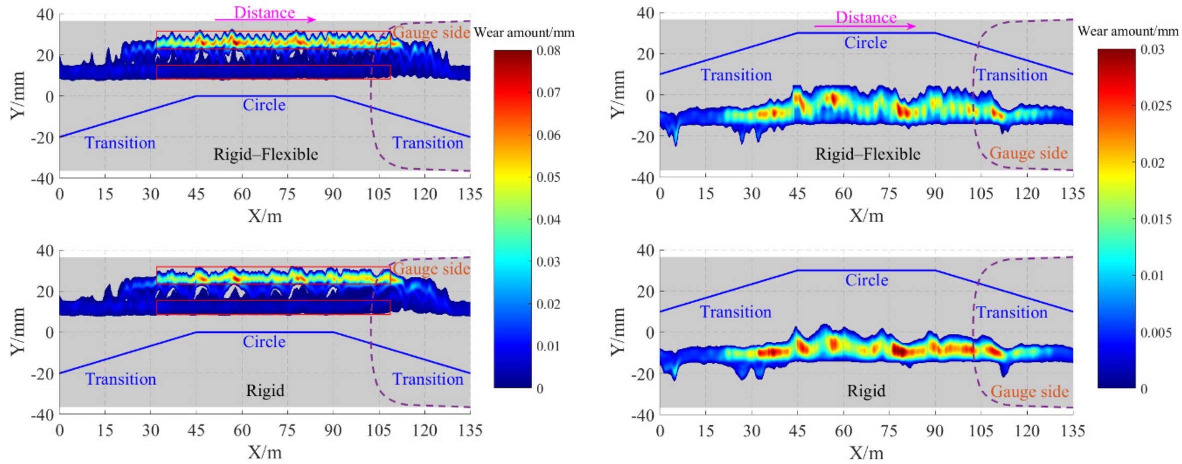

(**a**) High rail (**b**) Low rail

Figure 14. Rail wear band results after the 1st iteration (curved case).

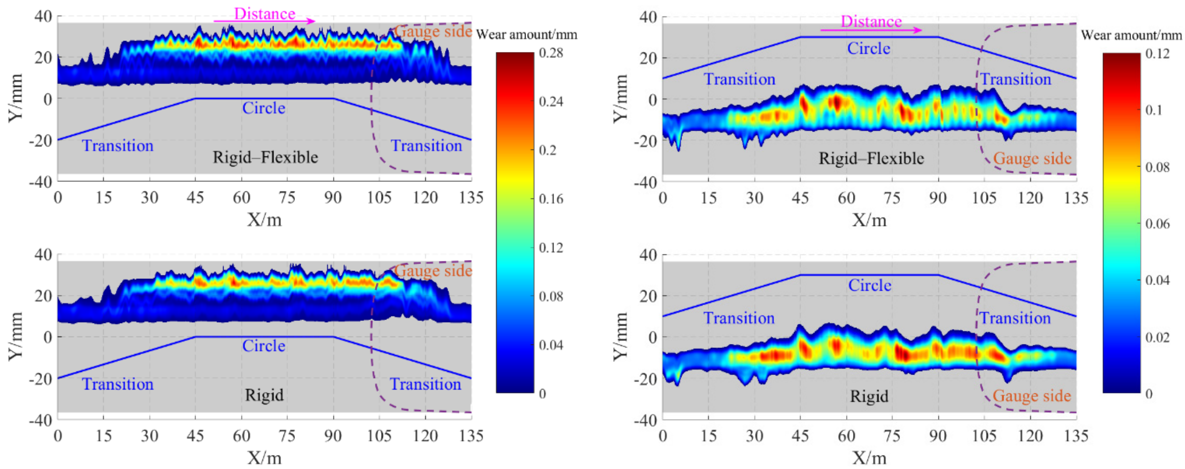

(**a**) High rail (**b**) Low rail

Figure 15. Rail wear band result after the 5th iteration (curved case).

To better illustrate the variations in rail wear at different longitudinal positions, a rigid-flexible coupled dynamic model is used as an example in Figure 16. This figure shows the maximum wear depth along the longitudinal position of different cross sections on both straight and circular rails. Since the rail wear is mainly caused by the leading wheelset, the figure contains black dashed lines indicating the wear numbers of the left (right) wheel on the leading wheelset, which can be calculated as the product of creep force and creepage. During the first iteration, the differences in maximum wear depth between the different cross sections are largely due to the track irregularities. As shown in Figure 16, the locations of pronounced wear remain relatively stable as the wear progresses, indicating that the influence of track irregularities is the main factor for the uneven longitudinal distribution of rail wear. The straight section, which has lower rail wear, shows larger variations in maximum wear depth over different longitudinal positions due to the influence of the track irregularities. There is also a strong correlation between the maximum wear depth on each cross section and the wear number at that position, with higher wear numbers corresponding almost exclusively to greater wear depths. The position of the contact point varies continuously with the wear of the steel rail, and the position of the contact point in the previous iteration may be in the noncontact region in the subsequent iteration, leading to differences in the growing trend of maximum wear depth on different cross sections.

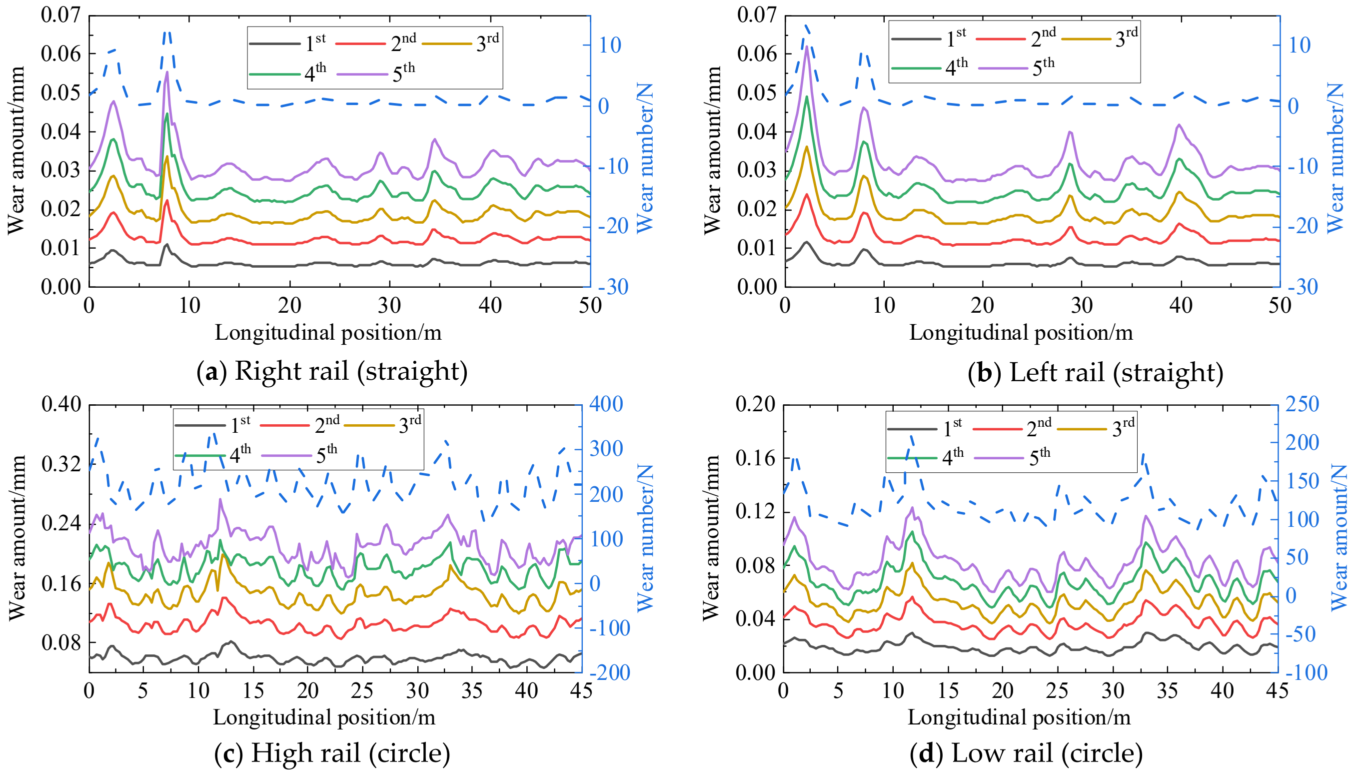

Figure 16. Longitudinal distribution of maximum wear depth of cross section under different iterations.

4.3. Rail Lateral Wear Distribution

Figure 17 compares the lateral wear distribution at a cross section of the straight and circular curve between the multibody dynamic model and the rigid-flexible coupled dynamic model for the first five iterations. The solid line represents the first model, while the dotted line represents the second model. Both models show a gradual increase in wear amount and wear area with increasing the number of iterations. However, the differences in the contact point positions determined by the two models lead to discrepancies in the wear area, wear depth, and lateral position corresponding to the maximum wear depth. Nevertheless, the overall wear characteristics and the shapes of the lateral wear distribution remain largely similar.

4.4. Wear Area

To further compare the differences in rail wear prediction between the two models, the differences in wear area at different longitudinal positions on both the straight and circular curve are examined. The results, shown in Figure 18, are obtained by integrating the wear distribution along the transverse position for each cross section. In the figure, the multibody dynamic model and the rigid-flexible coupled dynamic model are represented by solid and dashed lines, respectively. The results indicate a strong correlation between the longitudinal distributions of wear area and wear number in Figure 16, with larger wear areas corresponding to locations with larger wear numbers. The two models have similar distribution characteristics of wear area in the longitudinal direction, and the positions of prominent wear areas are essentially identical.

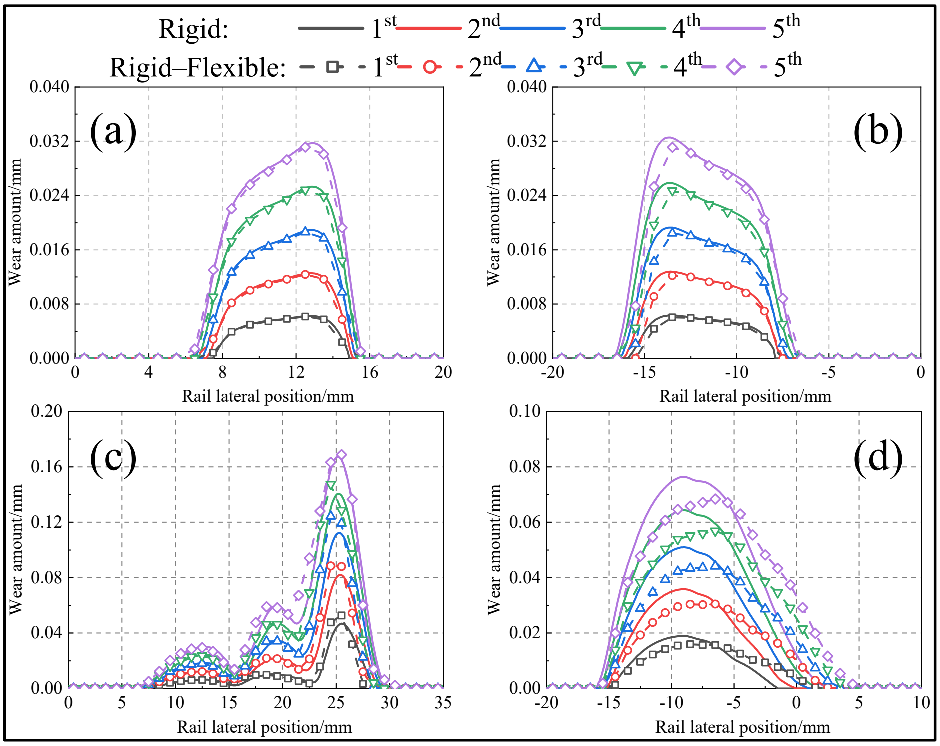

Figure 17. The results of rail lateral wear distribution: (**a**) Right rail (straight); (**b**) left rail (straight); (**c**) high rail (circle); (**d**) low rail (circle).

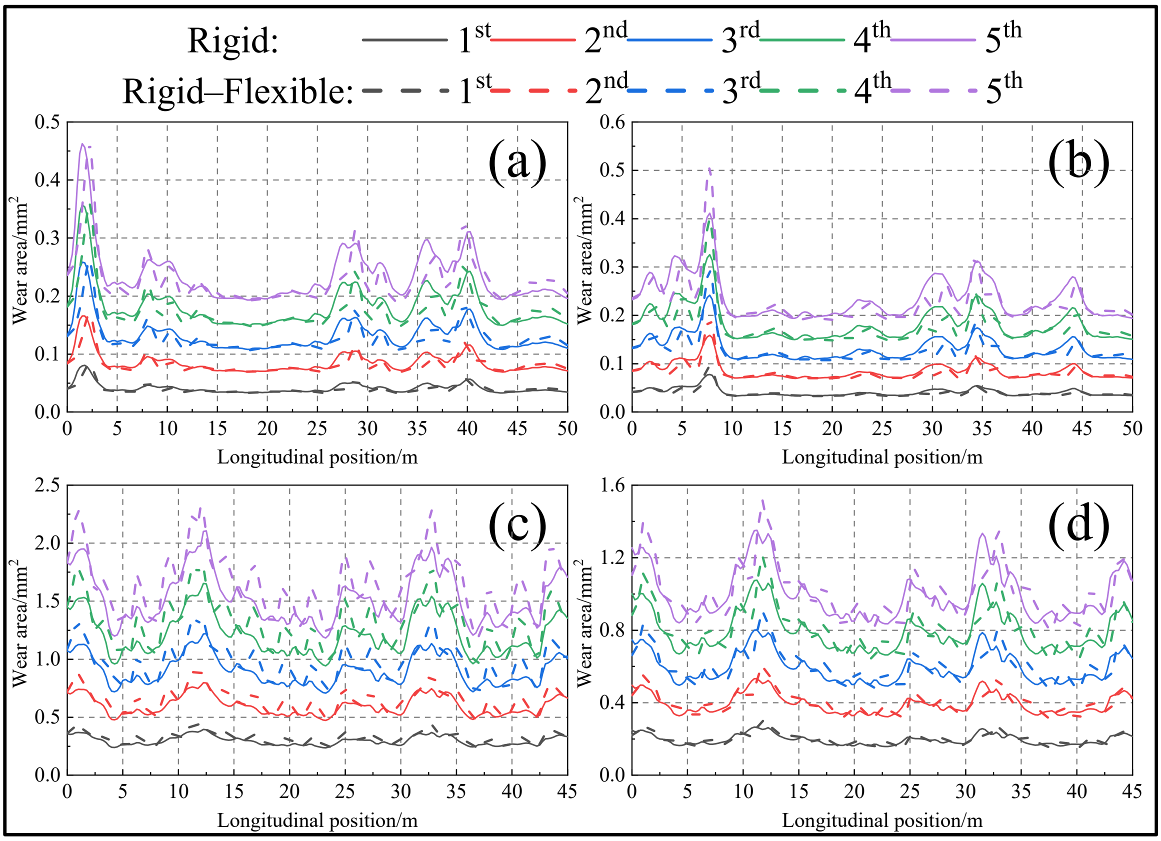

Figure 18. Distribution of wear area at different longitudinal positions: (**a**) Right rail (straight); (**b**) left rail (straight); (**c**) high rail (circle); (**d**) low rail (circle).

Figure 19 shows a comparative analysis of the differences between the two models in terms of mean wear area. Figure 19a,b show the mean wear area of all cross sections after each iteration for the curved and straight cases, respectively. For the curved case, the difference in wear area between the high and low rails increases as the number of iterations increases. The wear area shows a linear upward trend, and the mean wear area derived from the multi-rigid-body dynamic model is smaller than that from the rigid-flexible coupled dynamic model. In the first five iterations, the maximum deviation between the two models is 3.4%. In contrast, for the straight case, the average wear area of the left rail is almost the same as that of the right rail, suggesting similar wear level on both sides of the rail. As for the model comparison, the average wear area of the multi-rigid-body dynamic model is larger than that of the rigid-flexible coupled dynamic model. In the first five iterations, the maximum difference between the two models is 3.6%.

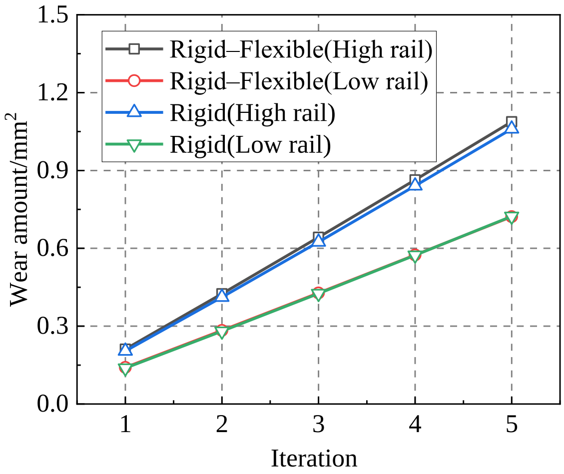

(**a**) curved case

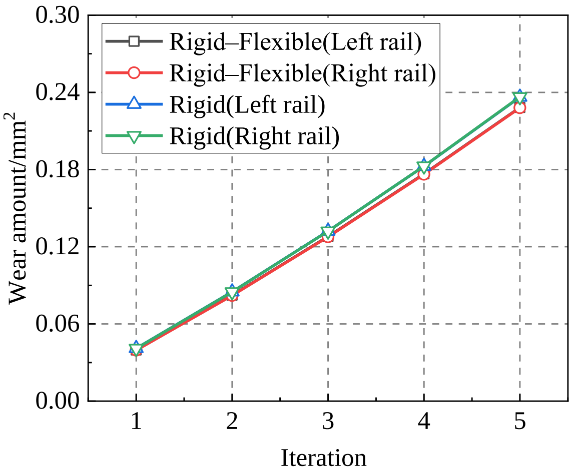

(**b**) straight case

Figure 19. Averaged result of wear area.

After a comprehensive comparative analysis of the position of the rail contact points, the wear distribution, and the wear area, it is found that the results of both the rigid-flexible coupled dynamic model and the multi-rigid-body dynamic model are similar. However, the rigid-flexible coupled dynamic model shows a significant increase in computational cost. To illustrate, in the straight track scenario, it takes about 30 h to simulate five wear cycles. In comparison, the multi-rigid-body dynamic model requires only about 15 min of simulation time. Considering the flexibility of the wheel–rail system has a significant impact on the simulation time. Therefore, considering the computational efficiency and accuracy, it is recommended to use the multi-rigid-body dynamic model for rail wear prediction simulations.

5. Conclusions

This study presents a rail wear prediction model that introduces a sampling strategy to evaluate the three-dimensional distribution of rail wear in the longitudinal and lateral directions. In addition, a rigid-flexible coupled dynamic model using SIMPACK and ANSYS is used to account for the structural flexibility of the wheelset and track. The results of the multi-rigid-body dynamic model and the rigid-flexible coupled dynamic model for predicting rail wear are compared. The main results of this study are presented below:

(1) For the case of straight track, the difference between the calculated positions of the rail contact points with the two models is relatively insignificant. In curves with small radius, some discrepancy is observed. This discrepancy can be attributed to the fact that the rigid-flexible coupled dynamic model takes into account the dynamic expansion of the track gauge, which, in turn, causes a larger lateral displacement of the wheelset compared to the multi-rigid-body dynamic model.

(2) The two models show relative similarity in terms of the three-dimensional wear distribution of the rail, with consistent prominent wear regions observed. The main difference between the two models is in the depth and range of wear, while the shape of the lateral wear distribution and overall wear characteristics remain essentially the same. In the first five iterations, the maximum percentage difference in the average wear area between the two models is 3.4% for the curved and straight track and 3.6% for the straight track.

(3) The track irregularity is the main reason for the uneven distribution of rail wear in the longitudinal direction. The wear band on the straight and circular tracks is relatively straight in the longitudinal direction. At the transition, differences in radius of curvature and superelevation at different longitudinal positions result in a trumpet-shaped wear band, and the region near the circular curve has higher wear and a wider wear range. The maximum wear depth and wear area on each cross section exhibit a

robust correlation with the wear number at the corresponding location. In addition, the areas of pronounced wear remain almost unchanged as the wear progresses.

(4) Considering the computational efficiency and accuracy, it is advisable to use a multi-rigid-body dynamic model to predict the rail wear.

Author Contributions: Methodology, B.W.; Formal analysis, B.W.; Writing—original draft, B.W.; Writing—review & editing, G.T. and Z.W.; Supervision, G.T. and Z.W.; Funding acquisition, X.W. and S.W. All authors have read and agreed to the published version of the manuscript.

Funding: The present work is supported by the National Natural Science Foundation of China (No. U21A20167), the Regional Innovation Cooperation Project of Sichuan Province of China (No. 2023YFQ0091), the Science and Technology Program of Guangxi Province of China (No. AD20297125), and the Science and Technology Projects of China National Accreditation Commission for Conformity Assessment (No. 2022CNAS15).

Data Availability Statement: Not applicable.

Conflicts of Interest: The authors declare no conflict of interest.

References

1. Jin, X. Research progress of high-speed wheel–rail relationship. *Lubricants* **2022**, *10*, 248. [CrossRef]
2. Wang, S.; Qian, Y.; Feng, Q.; Guo, F.; Rizos, D.; Luo, X. Investigating high rail side wear in urban transit track through numerical simulation and field monitoring. *Wear* **2021**, *470*, 203643. [CrossRef]
3. Venter, J.P. Investigation into the abnormally high wear rate of AC electric locomotive wheels on the Ermelo-Richards Bay coal line when replacing UIC-A rail with chrome-maganese rail. In Proceedings of the Fourth International Heavy Haul Railway Conference 1989: Railways in Action, Brisbane, Australia, 11–15 September 1989; pp. 551–556.
4. Bosso, N.; Magelli, M.; Zampieri, N. Simulation of wheel and rail profile wear: A review of numerical models. *Rail. Eng. Sci.* **2022**, *30*, 403–436. [CrossRef]
5. Shebani, A.; Iwnicki, S. Prediction of wheel and rail wear under different contact conditions using artificial neural networks. *Wear* **2018**, *406*, 173–184. [CrossRef]
6. Han, P.; Zhang, W. A new binary wheel wear prediction model based on statistical method and the demonstration. *Wear* **2015**, *324*, 90–99. [CrossRef]
7. Jendel, T. Prediction of wheel profile wear—Comparisons with field measurements. *Wear* **2002**, *253*, 89–99. [CrossRef]
8. Enblom, R.; Berg, M. Proposed procedure and trial simulation of rail profile evolution due to uniform wear. *Proc. Inst. Mech. Eng. Part F J. Rail Rapid Transit.* **2008**, *222*, 15–25. [CrossRef]
9. Jin, X.; Xiao, X.; Wen, Z.; Guo, J.; Zhu, M. An investigation into the effect of train curving on wear and contact stresses of wheel and rail. *Tribol. Int.* **2009**, *42*, 475–490. [CrossRef]
10. Ye, Y.; Sun, Y.; Shi, D.; Peng, B.; Hecht, M. A wheel wear prediction model of non-Hertzian wheel–rail contact considering wheelset yaw: Comparison between simulated and field test results. *Wear* **2021**, *474*, 203715. [CrossRef]
11. Zhu, A.; Yang, S.; Li, Q.; Yang, J.; Li, X.; Xie, Y. Simulation and measurement study of metro wheel wear based on the Archard model. *Ind. Lubr. Tribol.* **2018**, *71*, 284–294. [CrossRef]
12. Zhu, A.; Yang, S.; Li, Q.; Yang, J.; Fu, C.; Zhang, J.; Yao, D. Research on prediction of metro wheel wear based on integrated data-model-driven approach. *IEEE Access* **2019**, *7*, 178153–178166. [CrossRef]
13. Ding, J.; Li, F.; Huang, Y.; Sun, S.; Zhang, L. Application of the semi-Hertzian method to the prediction of wheel wear in heavy haul freight car. *Wear* **2014**, *314*, 104–110. [CrossRef]
14. Wen, B.; Wang, S.; Tao, G.; Li, J.; Ren, D.; Wen, Z. Prediction of rail profile evolution on metro curved tracks: Wear model and validation. *Int. J. Rail Transp.* **2022**, 1–22. [CrossRef]
15. Li, Y.; Ren, Z.; Enblom, R.; Stichel, S.; Li, G. Wheel wear prediction on a high-speed train in China. *Veh. Syst. Dyn.* **2020**, *58*, 1839–1858. [CrossRef]
16. Innocenti, A.; Marini, L.; Meli, E.; Pallini, G.; Rindi, A. Prediction of wheel and rail profile wear on complex railway networks. *Int. J. Rail Transp.* **2014**, *2*, 111–145. [CrossRef]
17. Hartwich, D.; Müller, G.; Meierhofer, A.; Obadic, D.; Rosenberger, M.; Lewis, R.; Six, K. A new hybrid approach to predict worn wheel profile shapes. *Veh. Syst. Dyn.* **2022**, 1–17. [CrossRef]
18. Ye, Y.; Qi, Y.; Shi, D.; Sun, Y.; Zhou, Y.; Hecht, M. Rotary-scaling fine-tuning (RSFT) method for optimizing railway wheel profiles and its application to a locomotive. *Rail. Eng. Sci.* **2020**, *28*, 160–183. [CrossRef]
19. Li, G.; Li, X.; Li, M.; Na, T.; Wu, S.; Ding, W. Multi-objective optimisation of high-speed rail profile with small radius curved based on NSGA-II Algorithm. *Veh. Syst. Dyn.* **2022**, 1–25. [CrossRef]
20. Shi, J.; Gao, Y.; Long, X.; Wang, Y. Optimizing rail profiles to improve metro vehicle-rail dynamic performance considering worn wheel profiles and curved tracks. *Struct. Multidiscip. Optim.* **2021**, *63*, 419–438. [CrossRef]

21. Gao, T.; Wang, Q.; Yang, K.; Yang, C.; Wang, P.; He, Q. Estimation of rail renewal period in small radius curveds: A data and mechanics integrated approach. *Measurement* **2021**, *185*, 110038. [CrossRef]
22. Jin, X.; Wu, P.; Wen, Z. Effects of structure elastic deformations of wheelset and track on creep forces of wheel/rail in rolling contact. *Wear* **2002**, *253*, 247–256. [CrossRef]
23. Zhai, W.; Wang, K.; Cai, C. Fundamentals of vehicle-track coupled dynamics. *Veh. Syst. Dyn.* **2009**, *47*, 1349–1376. [CrossRef]
24. Aceituno, J.F.; Wang, P.; Wang, L.; Shabana, A.A. Influence of rail flexibility in a wheel/rail wear prediction model. *Proc. Inst. Mech. Eng. Part F J. Rail Rapid Transit.* **2017**, *231*, 57–74. [CrossRef]
25. Tao, G.; Ren, D.; Wang, L.; Wen, Z.; Jin, X. Online prediction model for wheel wear considering track flexibility. *Multibody Syst. Dyn.* **2018**, *44*, 313–334. [CrossRef]
26. Shi, Z.; Zhu, S.; Rindi, A.; Meli, E. Development and validation of a wear prediction model for railway applications including track flexibility. *Wear* **2021**, *486*, 204092. [CrossRef]
27. Guo, T.; Qi, Y.; Gan, F. Simulation and analysis of wheel wear prediction with rigid flexible couple wheelset. *Conf. Ser. Earth Environ. Sci.* **2018**, *189*, 032012. [CrossRef]
28. Vila, P.; Fayos, J.; Baeza, L. Simulation of the evolution of rail corrugation using a rotating flexible wheelset model. *Veh. Syst. Dyn.* **2011**, *49*, 1749–1769. [CrossRef]
29. Baeza, L.; Vila, P.; Xie, G.; Iwnicki, S.D. Prediction of rail corrugation using a rotating flexible wheelset coupled with a flexible track model and a non-Hertzian/non-steady contact model. *J. Sound Vib.* **2011**, *330*, 4493–4507. [CrossRef]
30. Kalker, J.J. A Fast Algorithm for the Simplified Theory of Rolling Contact. *Veh. Syst. Dyn.* **1982**, *11*, 1–13. [CrossRef]
31. Guo, L. Study on Wear and Damage Behaviors and Wear Prediction of U75V Rail under Dry and Water Medium Conditions. Ph.D. Thesis, Southwest Jiaotong University, Chengdu, China, 2022. (In Chinese).
32. Enblom, R.; Berg, M. Simulation of railway wheel profile development due to wear—Influence of disc braking and contact environment. *Wear* **2005**, *258*, 1055–1063. [CrossRef]
33. Braghin, F.; Lewis, R.; Dwyer-Joyce, R.S.; Bruni, S. A mathematical model to predict railway wheel profile evolution due to wear. *Wear* **2006**, *261*, 1253–1264. [CrossRef]
34. Lewis, R.; Dwyer-Joyce, R.S. Wear mechanisms and transitions in railway wheel steels. *J. Eng. Tribol.* **2004**, *218*, 467–478. [CrossRef]
35. Lewis, R.; Olofsson, U. Mapping rail wear regimes and transitions. *Wear* **2004**, *257*, 721–729. [CrossRef]
36. Sun, Y.; Guo, Y.; Lv, K.; Chen, M.; Zhai, W. Effect of hollow-worn wheels on the evolution of rail wear. *Wear* **2019**, *436*, 203032. [CrossRef]
37. Sun, Y.; Guo, Y.; Zhai, W. Prediction of rail non-uniform wear—Influence of track random irregularity. *Wear* **2019**, *420*, 235–244. [CrossRef]
38. Guyan, R.J. Reduction of stiffness and mass matrices. *AIAA J.* **1965**, *3*, 380. [CrossRef]